INL/JOU-22-68797-Revision-0

Conversion kinetics during melting of simulated nuclear waste glass feeds measured by dissolution of silica

March 2022

Pavel Ferkl, Pavel Hrma, Alexander W Abboud, Donna Post Guillen, John Khawand, Ivan Kopal, Martina Kohoutkova, Miraslava Vernerova, Jaroslav Klouzek, Mark Hall, Albert Kruger, Richard Pokorny

Changing the World's Energy Future

INL is a U.S. Department of Energy National Laboratory operated by Battelle Energy Alliance, LLC

INL/JOU-22-68797-Revision-0

Conversion kinetics during melting of simulated nuclear waste glass feeds measured by dissolution of silica

Pavel Ferkl, Pavel Hrma, Alexander W Abboud, Donna Post Guillen, John Khawand, Ivan Kopal, Martina Kohoutkova, Miraslava Vernerova, Jaroslav Klouzek, Mark Hall, Albert Kruger, Richard Pokorny

March 2022

Idaho National Laboratory
Idaho Falls, Idaho 83415

http://www.inl.gov

Prepared for the
U.S. Department of Energy
Under DOE Idaho Operations Office
Contract DE-AC07-05ID14517

Conversion kinetics during melting of simulated nuclear waste glass feeds measured by dissolution of silica

Pavel Ferkl[1], Pavel Hrma[2], Alexander Abboud[3], Donna Post Guillen[3], John Khawand[4], Ivan Kopal[4], Martina Kohoutková[4], Miroslava Vernerová[4,5], Jaroslav Kloužek[4,5], Mark Hall[1], Albert A. Kruger[6], Richard Pokorný[4,5]

[1] Pacific Northwest National Laboratory, Richland, WA 99354, United States of America

[2] AttainX, Support Services Contractor to the Office of River Protection, U.S. Department of Energy, Richland, WA 99354, United States of America

[3] Idaho National Laboratory, MS 3553, 995 University Blvd., Idaho Falls, ID 83415, United States of America

[4] Laboratory of Inorganic Materials, University of Chemistry and Technology Prague, Prague 6, 166 28, Czech Republic

[5] Institute of Rock Structure and Mechanics, Czech Academy of Sciences, Prague 8, 182 09, Czech Republic

[6] U.S. Department of Energy, Office of River Protection, Richland, WA 99354, United States of America

Abstract

We experimentally investigated the batch-to-glass conversion kinetics of two low-activity and two high-level nuclear waste melter feeds that represent widely different behavior during melting; tests comprised thermogravimetric analysis, the feed expansion test, evolved gas analysis, and x-ray diffraction. Our study indicates that the conversion processes, which include gas-evolving reactions, dissolution of crystalline phases, and primary foam expansion and collapse, are interconnected and influenced by the feed's thermal history. The fraction of dissolved silica was adopted as a measure of the extent of conversion inside the cold cap—the floating layer of feed material on the top surface of the melt in an electric melter. The interface between the cold cap and the free-flowing melt below was associated with a constant fraction of dissolved silica. The estimated viscosity of glass-forming melt at this interface lies within a narrow range for the feeds studied.

Keywords: vitrification; nuclear waste; kinetics; modeling; foaming; processing

1. Introduction

For decades, mathematical models of glass melting furnaces have been employed to enhance the production efficiency and improve the product quality [1–10]. To obtain the glass production rate, i.e., the rate of melting, as a model output, a model for the feed-to-glass conversion as it occurs in the cold cap, the mass of material that floats on the glass melt surface, is needed [11–13]. Computational fluid dynamics (CFD) models were recently developed for Joule heated melters designed to vitrify high-level and low-activity radioactive wastes (HLW and LAW, respectively), in the Waste Treatment and Immobilization Plant at the Hanford Site in the U.S. state of Washington [14–19]. To couple the cold cap model with the CFD melter model, the interface between the cold cap and the melt must be well-defined. The temperature at the interface (the cold cap bottom temperature) is linked to the feed-to-glass conversion kinetics, which in turn depends on the thermal history the feed experiences as it passes through the cold cap.

The melter feed is composed of nuclear waste and glass-forming/modifying minerals and chemicals. Conversion of this chemically complex mixture to glass is rather complicated: condensed

materials, solid and molten, move downward through the cold cap while undergoing multiple, interdependent conversion reactions, including water evaporation [12,20,21], creation of molten salt phase [22–24], evolution of gases [25,26], dissolution of refractory particles [27,28], and foam growth and collapse [13,29–31]. Detailed description would be rather unwieldy, not to mention that experimental data are lacking and the theoretical understanding is incomplete. The method originally developed for a commercial glass batch [32,33] provides a simple approach: the degree of conversion is gauged using the extent of silica dissolution.

The feed-to-glass conversion process in the glass melter is maintained in a steady state through the steady-state heat fluxes delivered to the top and bottom of the cold cap. The heat flux to the cold cap bottom, which controls the rate of melting, depends on the cold cap bottom temperature, T_B, which is a function of conversion kinetics [34–36]. This temperature has been estimated using data from the feed expansion test (FET) and evolved gas analysis (EGA). Both methods have drawbacks (see Section 5). Recent studies [32,33] indicate that although silica dissolution is affected by the heating rate, the dissolved silica fraction, f_B, reached at T_B is independent of temperature history. Based on these results, we measured, using x-ray diffraction (XRD), the dissolved silica fraction in samples heated at 2 to 30 K min^{-1}. Then we fitted semiempirical kinetic models of silica dissolution and determined the f_B value at which the temperature equals the T_B obtained from FET and/or EGA. In this study, we apply this method to feeds with widely different melting behavior.

Section 2 describes the experimental methods used to collect the kinetic data of the feed-to-glass conversion process. Section 3 details the mathematical model employed for silica dissolution kinetics. Section 4 presents the results and discusses the effects of feed composition and thermal history on the conversion kinetics, cold cap bottom temperature, and melt viscosity. Section 5 provides additional context on techniques for assessing T_B.

2. Experimental Methods

The melter feeds and glasses employed in this study were designed to vitrify Hanford HLW and LAW streams. Based on their widely different behavior during melting, four such feeds were selected for the present study: high-alumina feed for HLW (denoted HLW-Al-19) [37], high-iron feed for HLW (HLW-NG-Fe2) [38], high-sodium AN-105 feed for LAW (LAW-AN105) [39], and low-sodium AZ-102 feed for LAW (LAW-AZ102) [40]. The compositions of these feeds and glasses are listed in the appendix, Tables A1 and A2. To investigate and mathematically formulate the conversion process of these feeds, the following experimental methods were used: XRD, thermogravimetric analysis (TGA), the FET, and EGA.

Samples for XDR, TGA, and FET were heated at 2, 5, 10, 20, and 30 K min^{-1} (for EGA, the 30 K min^{-1} heat treatment was not performed) over the temperature range from room temperature to 1150 °C under the air atmosphere for XRD and FET, argon for TGA, and helium for EGA. Samples were placed in porcelain crucibles for XRD, in alumina crucibles for TGA, and in quartz glass tubes for EGA; FET samples are heated on alumina plate.

2.1 X-Ray Diffraction

The XRD was performed to measure fractions of crystalline phases in heat-treated 4 g samples of the feeds to maximum temperatures between room temperature and 1200 °C in 100 °C increments. After reaching the desired temperatures, samples were air quenched, ground in a planetary ball mill

(Fritsch P6, 10 grinding balls, 4 min, 300 rpm), and crushed to under 100 μm grain size. Approximately 1 g samples were treated in the XRD diffractometer (PANalytical X'Pert^3 Powder) using continuous scan type, 5 to 80° 2θ angular range, 0.04° step size, 115 s scan step, Cu Kα anode, 40 kV, 30 mA generator settings, PIXcel1D detector (Malvern), and a ring-shaped holder with internal diameter 27 mm at 25 °C. Rietveld refinement was carried out using Highscore Plus software and amorphous fractions were obtained using the external standard method with SiO_2-quartz as the standard.

2.2 Thermogravimetric Analysis and Evolved Gas Analysis

TGA and EGA are complementary methods for gas evolution kinetics. Unlike TGA, the EGA is sensitive enough to detect gases as they continue to evolve in tiny amounts during primary foam collapse, but the long sampling period, ~60 s, of the gas separation step in the chromatograph makes it difficult to capture fast events, such as bursting of individual bubbles.

For TGA (Setaram Setsys), the sample mass was 30 mg. For EGA, a gas chromatograph with a mass spectrometric detector (Agilent 6890N/5973N) was used to measure the evolution rate of individual gases (except water, which condenses on tube walls and piping) during heating of 1 g samples. The carrier gas was flowing at 50 mL min^{-1} [41]. The gas evolution rate was obtained from the concentration of the *i*th gas in the carrier gas as , where c_i is the *i*th gas fraction in the carrier gas, is the carrier gas (He) flow rate, is the *i*th gas molar mass, m is the batch sample mass, n is the gas molar volume (n = 22,410 mL per mole), and Φ is the heating rate.

2.3 Feed Expansion Tests

The FET measures the feed volume and porosity as functions of temperature [42]. A feed sample of 0.5 g was uniaxially pressed (170 MPa) into a pellet 13 mm in diameter. During the heat-treatment, images of pellets were recorded through a window in the furnace wall. Assuming the sample is axially symmetric, an algorithm in NIS-Elements® (Laboratory Imaging, Czech Republic) software then evaluated sample volumes from sample profile areas.

3. Kinetic Modeling

The cold cap bottom—the geometric boundary between the reacting feed and the molten glass below—is located at the surface at which primary foam is collapsing (see Fig. 1). The foam collapsing temperature is estimated based on the peaks on the volume-versus-temperature curves measured with FET. According to the height and shape of these peaks, we distinguish among three basic types of primary foam: moderate, strong, and vigorous (see foaming curves displayed in Sections 4.2 and 4.3).

Moderate foams typically produce a sharp peak with maximum foam porosity smaller than 0.75. By EGA, little gas evolution is observed between the foam onset temperature, T_{FO}, and the temperature of foam maximum, T_{FM}, as most gases are trapped inside the expanding foam and released only after the temperature exceeds T_{FM}. An example of this behavior is foaming of Al-19 feed.

Strong foams, represented by NG-Fe2 feed, typically produce sharp peaks with a maximum greater than 0.75. By EGA, a minor amount of gas is evolved between T_{FO} and T_{FM}.

For vigorous foams, like that observed in AN-105 feed, the peaks are blunt, often with several maxima and porosity in excess of 0.75. By EGA, large amounts of primary gases are released throughout the foaming interval. The foaming of these feeds resembles boiling liquid.

The type of primary foaming affects the cold cap bottom temperature, T_B, which has crucial effects on the rate of melting (see Section 5), because it directly affects the driving force for heat transfer from the melt into the cold cap. Although it is practically impossible to measure T_B directly in the melter during steady-state melting, T_B has been experimentally assessed in two ways [18,35,36]: (i) from the FET volumetric measurements, as the temperature at which growth of primary foam stops and the foam collapses, and (ii) from EGA, as the temperature at which vigorous primary gas evolution stops and secondary gases (O_2 and SO_2) start to evolve. The FET was used for feeds showing moderate or strong foaming, which exhibit a well-defined primary foam collapse, while EGA was used for vigorously foaming feeds for which the FET method was inadequate. AZ-102 feed does not fully conform to these patterns as it has small maximum porosity and releases only a small amount of gas between T_{FO} and T_{FM} that is typical for moderately foaming feeds, but it simultaneously has a blunt FET peak of a stable foam that does not collapse until the melt viscosity decreases sufficiently.

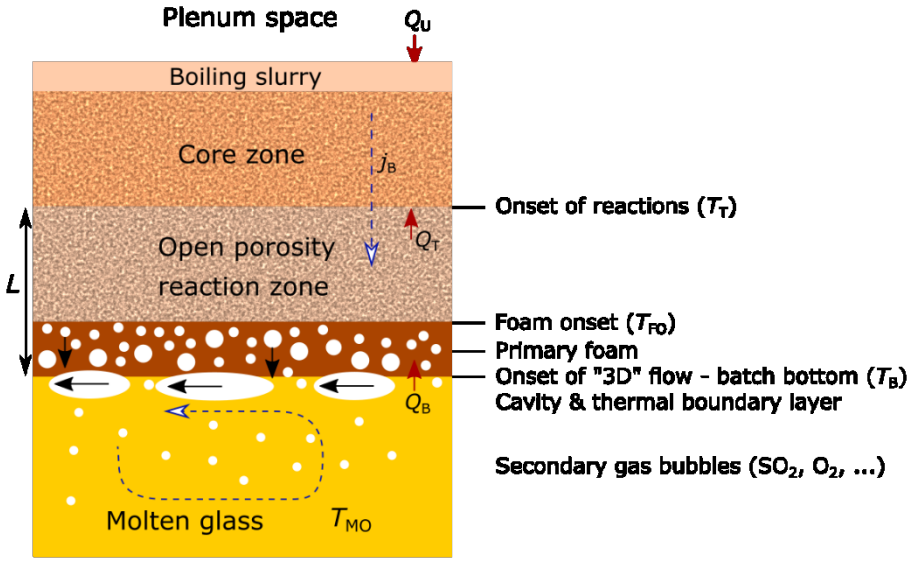

Figure 1. Schematic illustration of the cold cap in an electric melter. Heat for feed-to-glass conversion is delivered to the top and bottom of the cold cap. Slurry feed is charged on the cold cap top. The top surface is partially covered by the boiling slurry. The middle layers consist of dry feed with open porosity. Primary foam is at the bottom of the cold cap. The gas from collapsed foam coalesces into large bubbles that escape through vent holes or at the edges of the cold cap.

The effect of a constant heating rate, i.e., a linear thermal history, on the primary foam evolution and collapse, and thus the T_B value, has been investigated [43]. A full kinetic model is needed for a cold cap with a nonlinear thermal history. Using the fraction of dissolved silica as a measure of the extent of conversion, we have formulated a semiempirical model based on XRD data. The model is based on the general kinetic equation

(1)

where is the fraction of dissolved silica, is the temperature, is the time, is the SiO_2 fraction in the final glass, is the solid (i.e., undissolved) silica mass fraction in the feed with respect to the final glass, and the approximation function represents a model whose coefficients are determined by fitting to experimental data.

For experiments that are conducted at a constant rate of heating,, we were seeking a solution of Eq. (1) in the form

(2)

in which a sum of stretched exponential functions appeared acceptable for fitting to XRD data:

(3)

where [32]

(4)

where , , , and are adjustable parameters and is the number of terms necessary for fitting Eqs. (3) and (4) to data.

For feeds NG-Fe2 and AN-105, one term was sufficient in Eq. (3) (). For feeds Al-19 and AZ-102, two terms were necessary in Eq. (3) (). The values of adjustable parameters were obtained by fitting Eqs. (3) and (4) to data for T between 300 and 1100 °C and between 2 and 30 K min^{-1}.

For a wider range of temperature histories, the conversion kinetics must be described in the form of a rate equation, i.e., Eq. (1). Following a previous study [32], we selected the Šesták-Berggren equation [44,45] as a suitable form:

(5)

where is the universal gas constant and , , , and are the adjustable parameters of the ith term determined by the nonlinear least-squares method. By Eq. (3), the rate equation for silica dissolution becomes

(6)

At lower temperatures, approximately by 700 °C, silica dissolution is accelerated by the vigorous gas-evolving reactions; at later stages, silica is being dissolved in the glass-forming melt by multicomponent diffusion [46]. Hence, at least two terms are expected to govern the process, one for the initial reaction-controlled phase and the other for the final diffusion-controlled phase. Interestingly, only one term was needed for feeds NG-Fe2 and AN-105 (see Section 4.5).

To obtain adjustable parameters for Eq. (6), we computed the dissolution rate using the first derivative of function , Eq. (3), with respect to temperature:

(7)

4. Results

4.1 Thermogravimetric Analysis

Primary foam is produced by gases released in the temperature interval between T_{FO} and T_B (see Fig. 1). Fig. 2 displays the TGA mass fraction, , where is the sample mass at and is the final mass of glass at 800 °C, together with the gas evolution rate, , for each type of feed. Because the feeds are hygroscopic, initial values may differ slightly in repeated experiments. The gas evolution rate is close to zero near 800 °C, a temperature above which samples start to lose weight only by glass melt volatilization. Residual gases that cause foaming (Sections 4.2 and 4.3) are barely detectable by TGA. As expected, the peaks of the gas-evolving reactions shift to higher temperatures with higher heating rates [25,47]. The gas-evolving reactions of the major peaks were identified with the help of EGA data in Section 4.3. The total amount of mass lost ranges from 10 to 25 %, increasing in the order AZ-102 < NG-Fe2 < Al-19 < AN-105.

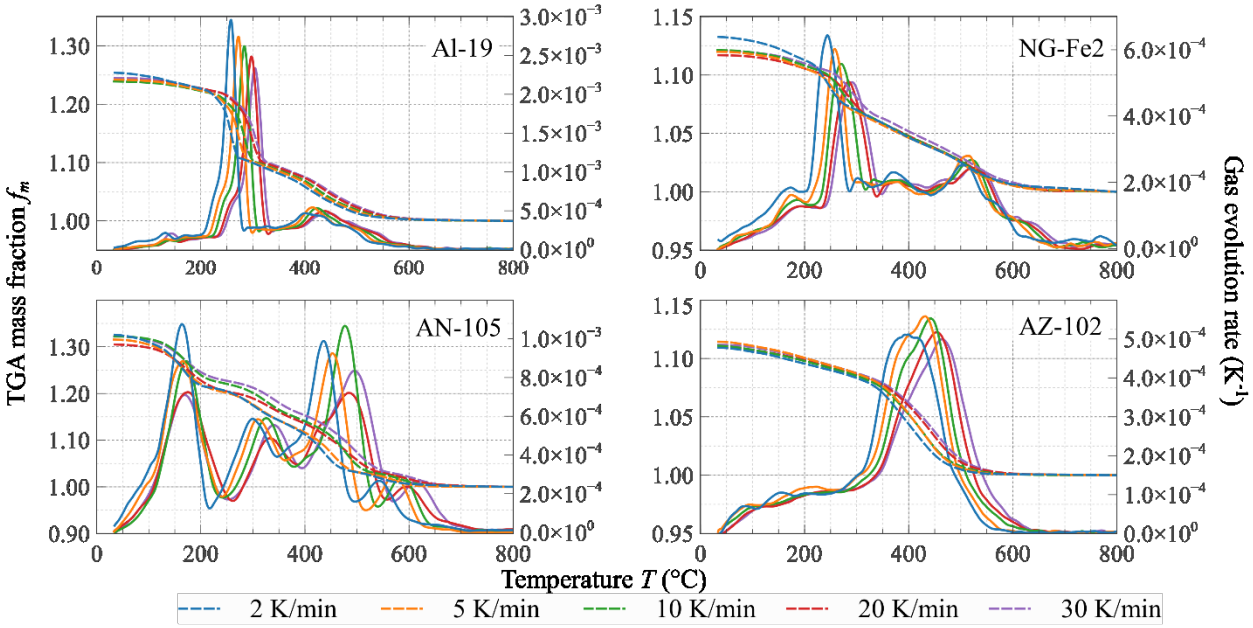

Figure 2. TGA mass fractions (dashed lines) and gas evolution rates (solid lines) versus temperature (left axis) and heating rate (right axis). Mass fraction is related to the glass product (for the final glass) and its initial value may be affected by sample humidity.

4.2 Feed Expansion Tests

Fig. 3 displays the normalized volume (V/V_g) of the feed pellets as a function of temperature, T, and heating rate, Φ, where V is the sample volume and V_g is the volume of the bubble-free glass melt. For illustration, also displayed are the profile images of feed pellets heated at 10 K min^{-1} captured at room temperature, at T_{FM}, and at 1050 °C (after the foam collapsed).

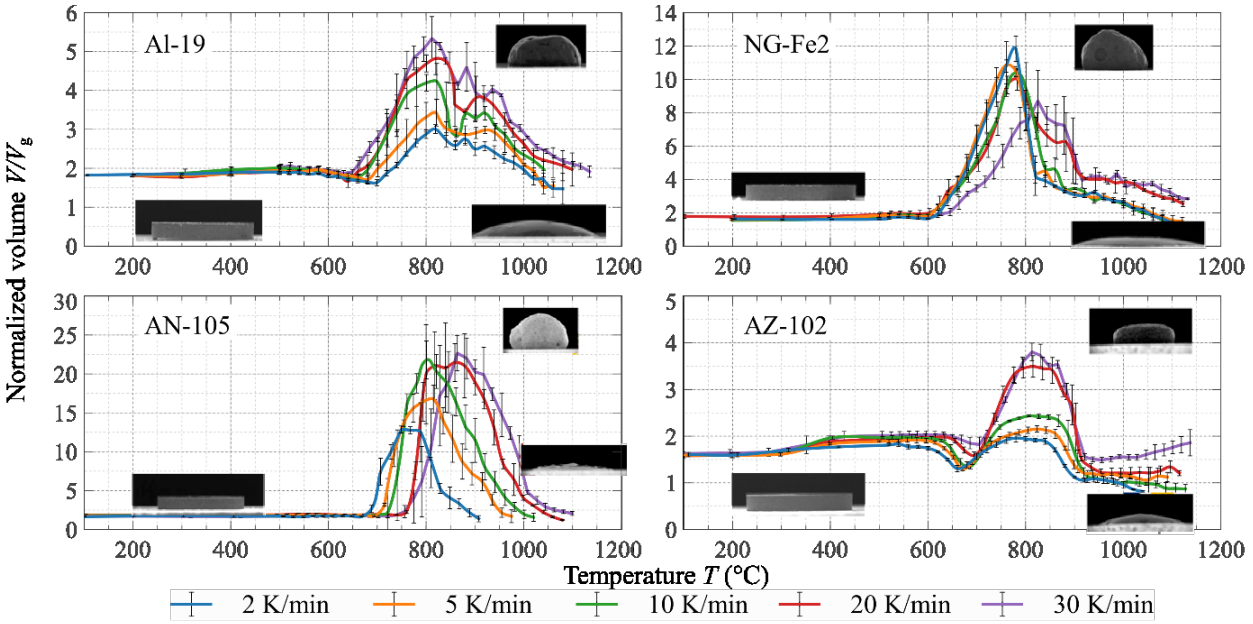

Figure 3. Normalized volume of loose batch versus temperature and heating rate, with profile images, of feed pellets heated at 10 K min^{-1}. When the normalized volume at temperatures above 1100 °C is greater than 1, the melt contains secondary bubbles.

Primary foam starts to evolve when enough glass-forming melt is produced and its viscosity becomes low enough to close open porosity and trap evolving gases, leading to volume expansion of the sample. Depending on the heating rate and the feed investigated, foam begins to grow at a temperature between 600 and 750 °C. As Fig. 4 shows, T_{FO} decreases with increasing heating rate for Al-19 feed and increases for NG-Fe2, AN-105, and AZ-102 feeds.

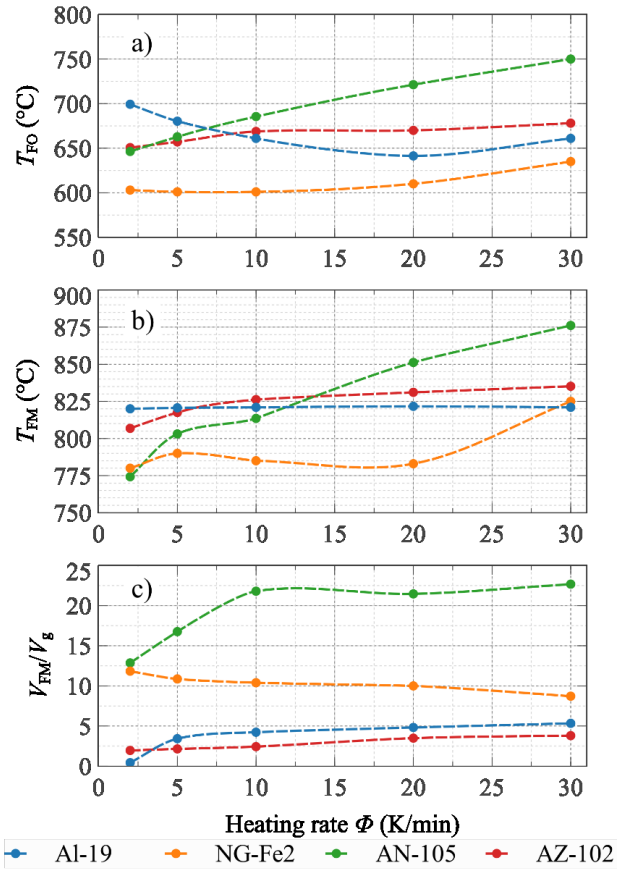

Figure 4. (a) T_{FO}, (b) T_{FM}, and (c) V_{FM}/V_g versus heating rate. Points show data; lines guide the eye. The values of T_{FO} and T_{FM} were determined by minimum and maximum values of a fitted third degree polynomial to data covering minimum and maximum values on the FET curve [43].

To understand the differences in the T_{FO} response to the heating rate, let us consider the effects of dissolved silica on the fraction of glass-forming melt and its viscosity. In a heated alkali-borosilicate melter feed, an alkali-borate melt forms before silica starts to dissolve. Its viscosity is initially low and decreases as temperature increases, but its volume fraction is too small to close porosity. The critical volume fraction of melt to close open pores is reached only when enough silica is dissolved. Since both viscosity and the glass-forming melt fraction increase simultaneously when silica is dissolving, the T_{FO} response to the heating rate depends on which effect is dominant at that stage: the effect of dissolving silica on the glass-forming melt viscosity or its effect on the fraction of glass-forming melt.

If the dissolving silica causes the viscosity to sharply increase before the critical volume fraction is reached, the porosity closure is limited by the decrease in viscosity by increasing temperature. But this may not be the case at a higher heating rate; the melt fraction remains low, because silica dissolution is relatively slow. Then the T_{FO} decreases as the heating rate increases for such feeds. This is probably the case for Al-19 feed (Fig. 4).

On the contrary, NG-Fe2, AN-105, and AZ-102 feeds are unlikely to contain large enough initial fractions of alkali-borate melt for early porosity closure (see Table A2) and need more silica dissolved to increase the melt volume. The silica dissolution process being relatively slow, the critical fraction of glass-forming melt is reached at a higher temperature when heating is faster. Thus, T_{FO} increases as the heating rate increases for these feeds. The real situation is even more complicated, because the rate of dissolution of alumina also plays an important role [48]. Moreover, the grain sizes of silica, alumina, and other raw materials have a decisive influence: the smaller the grain size, the faster they dissolve [49,50].

As temperature increases above T_{FO}, the sample volume increases until it reaches the maximum volume, V_{FM}, at temperature T_{FM} (~800–900 °C), above which the volume decreases as primary foam gradually collapses. Both V_{FM} and T_{FM} typically increase with increasing Φ as the gas-evolving reactions are shifted to higher temperatures (Fig. 4b), thus trapping more gases above T_{FO}. An earlier closure of pores results in more gas being trapped in the rising foam. However, the foam volume cannot grow arbitrarily high because it is limited by foam stability. Moderate foam collapses when viscosity decreases to 50–70 Pa s (Section 4.7), but vigorous foaming resembles boiling: excess gas is released without creating a distinct foam maximum.

Foam volume of AN-105 feed increases with increasing Φ up to 10 K min^{-1}, then remains virtually unchanged (Fig. 4c). An abrupt increase in AZ-102 foam volume at 20 K min^{-1}, seen in Fig. 3, is difficult to understand; it could be related to the shift of the residual CO_2 evolution into the primary foaming region (see Section 4.6). As to NG-Fe2 feed, a gradual decrease of V_{FM} with Φ followed by an abrupt decrease at 30 K min^{-1}, seen in Fig. 3, could result from a combination of multiple factors, including redox reactions, melt viscosity, and the presence of solid particles. It should be noted that Lee et al. [43] reported increasing V_{FM} for NG-Fe2 with Φ up to 40 K min^{-1}. The differences are likely caused by the different sources of feed materials [48].

As temperature increases further, the iron redox reaction and sulfate decomposition produce secondary bubbles that can cause secondary maxima on FET curves. More details about FET results can be found in references [51–55].

4.3 Evolved Gas Analysis

Fig. 5 overlays curves for the normalized volume determined by FET, gas evolution rate determined by TGA, and the gas evolution rates of O_2, NO, CO_2, and SO_2 determined by EGA at 10 K min^{-1} (detected small amounts of CO, N_2O, and N_2 are not displayed). In agreement with the TGA data, most gases evolve below T_{FO}. The main gas-evolving reactions are dehydration of hydrates and oxyhydrates (evolution of H_2O), reaction of nitrates and nitrites with organics (evolution of NO and CO_2), decomposition of carbonates (evolution of CO_2), decomposition of nitrates and nitrites (evolution of NO and O_2), decomposition of sulfates (evolution of SO_2 and O_2), and multivalent oxides redox reactions (evolution of O_2).

Minor gases, N_2, N_2O, and CO, evolve depending on the feed redox. Nitrogen did evolve at temperatures below 500 °C from AN-105 feed, to which sucrose was added to obtain the organic carbon-to-nitrogen ratio of 0.75.

Comparing gas evolution rates from TGA and EGA in Fig. 5, we attributed the main peaks of TGA gas evolution rate data to evolving gases: peak 1 in all feeds (a double peak in NG-Fe2) is attributed to water release (not detected in EGA setup, see Section 2.2) and all other peaks to CO_2, NO,

and O_2 in various proportions.

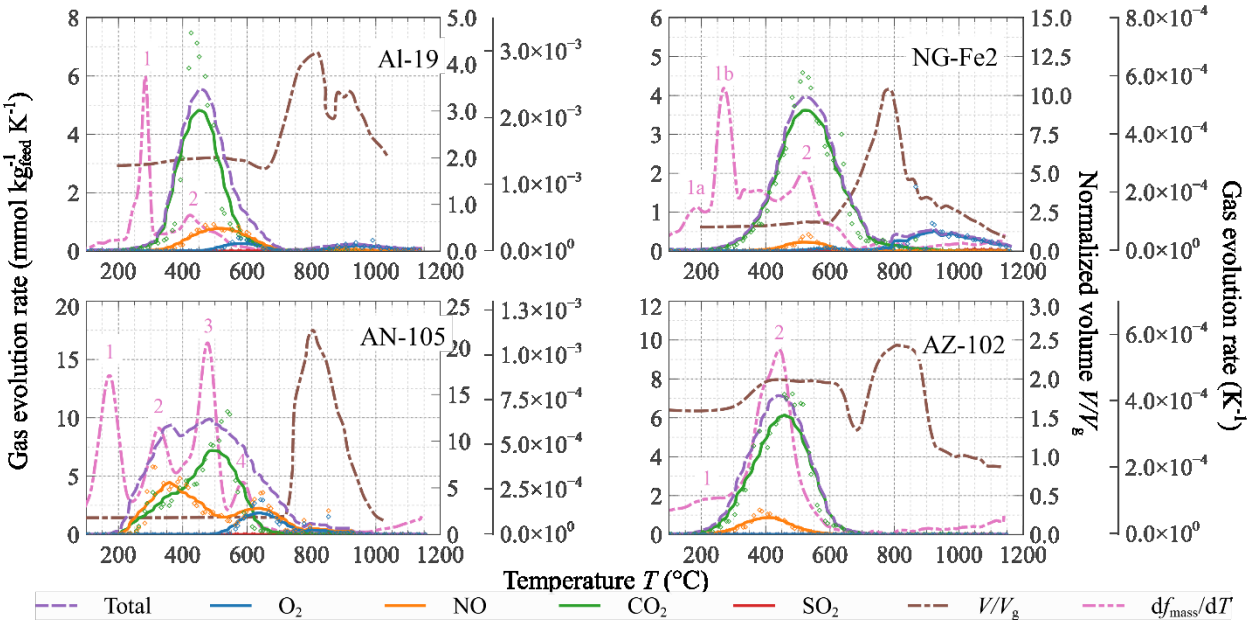

Figure 5. The individual (solid lines) and total (dashed lines) gas evolution rates versus temperature together with the feed volume normalized to the volume of final glass measured by FET (dash-dotted lines) and TGA gas evolution rate (dash-dot-dot lines). The numbers at major peaks label TGA gas evolution rates. For EGA gas evolution rates, the lines correspond to measured data filtered by centered moving average (5 points on either side).

4.4 Silica Dissolution (XRD)

Melter feeds contain fluxes, such as alkali and alkaline-earth hydroxides, carbonates, or nitrates, and refractories, such as silica, alumina, or zirconia. On heating, a molten salt phase appears at a temperature as low as 200 °C [24,56,57]. This melt, also called primary melt, has low viscosity and is highly reactive. It reacts with boric acid already in the aqueous medium of the feed slurry and continues reacting during feed slurry drying, creating an early amorphous borate phase. During subsequent heating, the solid components react, partially turning to secondary crystalline phases and eventually dissolving in the glass-forming melt, which acts as a solvent. The XRD patterns and the responses of the major quartz peak to heating are shown in Supplement, Fig. S1. The fractions of crystalline phases in the nonvolatile portion of the feeds (the final glass mass) were obtained from the raw data using the TGA mass fraction defined in Section 4.1. The dissolution of silica, the major crystalline phase in each feed, is described in Section 4.5.

Based on XRD data, Fig. 6 displays the evolution of crystalline phases other than quartz in feed samples heated at 10 K min^{-1}. As temperature increases, gibbsite ($Al(OH)_3$) turns into boehmite (AlO(OH)) by 500 °C in HLW feeds and is no longer detected at 300 °C in AN-105 feed. By 600 °C, boehmite turns into amorphous alumina that dissolves in the borate melt [24,56,58]. Similarly, iron hydroxide turns into hematite (Fe_2O_3) last detected at 800 °C in HLW feeds and at 600 °C in LAW feeds. Hematite then partly dissolves in the borate melt and partly turns into spinel, a solid solution of Ni, Cr and Mn oxides and magnetite (Fe_3O_4), which slowly dissolves on heating, but survives in the Al-19, making solid inclusions in the final glass [28].

The mineral components wollastonite ($CaSiO_3$), kyanite (Al_2SiO_5), zircon ($ZrSiO_4$), anatase (TiO_2), zincite (ZnO), and forsterite (Mg_2SiO_4) gradually dissolve in the glass-forming melt, anatase by 500 °C, zincite by 600 °C, wollastonite by 700 °C, kyanite and forsterite by 900 °C, and zircon by 1100 °C.

Several crystalline phases precipitate and later dissolve during the conversion process. Some may precipitate on cooling. Crystalline borates are not detected by XRD in the dry melted feed [56,59,60], but transient alkali silicate, borosilicate, alumino-borate, and alumino-borosilicate crystalline phases were detected at higher temperatures, typically dissolving by 900 °C [24,43,46,56]. They likely form within the concentration layers around dissolving silica particles: tincalconite ($Na_2B_4O_5(OH)(H_2O)_2$) in Al-19 and two minerals of sodalite structure, $Na_8(AlSiO_4)_6(NO_2)_2$ in AN-105 and $Na_8Al_6(SiO_4)_6(BF_4)_2$ in Al-19; the tincalconite and NO_2-sodalite phases first appeared at 300 °C; the BF_4-sodalite phase first appeared at 600 °C. Several salts, Li_2CO_3, $NaNO_3$, and $NaNO_2$, precipitated from the primary melt by 600 °C ($Al(NO_3)_3$•$9H_2O$ in AN-105 reacted with NaOH, forming $NaNO_3$. last detected at 600 °C). Lithium silicate (Li_2SiO_3), seen from 400 to 600 °C in AZ-102, was a likely intermediate reaction product of lithium carbonate with silica. Fluorapatite ($Ca_5(PO_4)_3F$) and aegirine ($NaFeSi_2O_6$) were detected between 700 and 900 °C. Silica started to dissolve in the borate glass-forming melt above 500 °C. Crystalline solids eventually dissolve in molten glass; spinel is an exception: tiny spinel crystals are dispersed in Fe-containing HLW glasses [61].

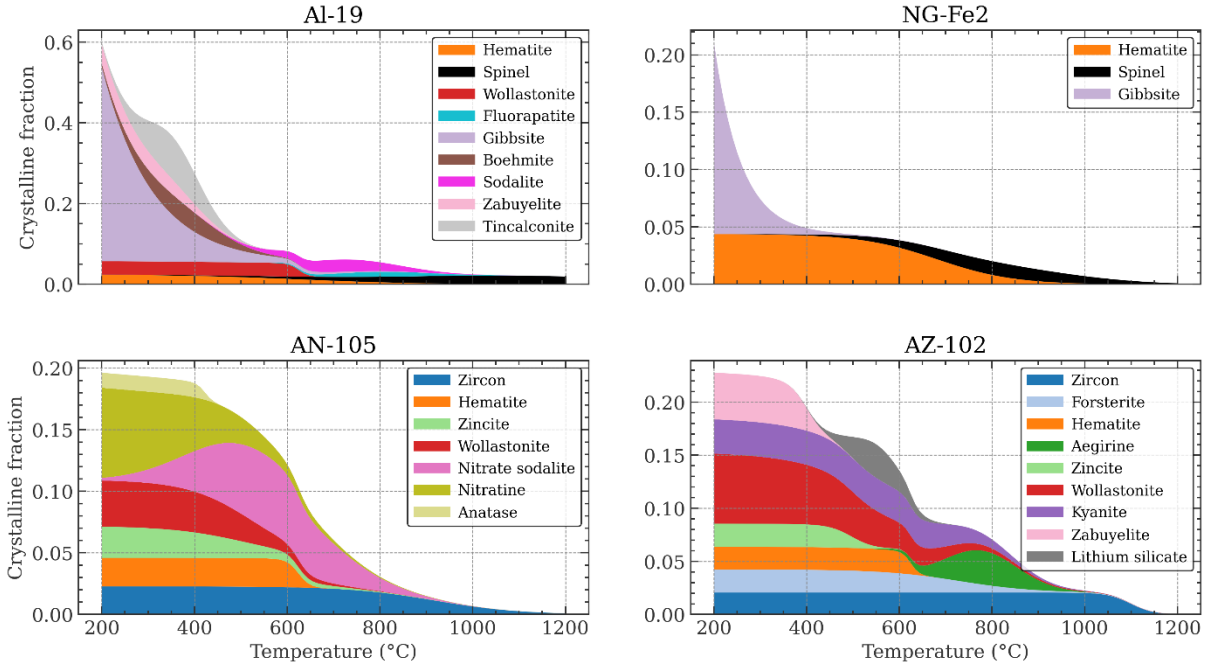

Figure 6. Evolution of crystalline phases other than quartz in feed samples heated at 10 K min^{-1}. Data was smoothed by fitting sigmoidal function to phases that were either increasing or decreasing over the whole temperature interval and gaussian function to the rest of the phases.

4.5 Kinetic Modeling of Silica Dissolution

As explained in Section 3, silica dissolution data were adopted to define the conversion progress inside the cold cap. The direct fitting of the kinetic model, Eq. (6), to the sparse, discrete values of fraction of dissolved silica, *f*, was not successful, requiring first the fitting of an empirical continuous

function, Eq. (3), that provided the dissolution rates in the kinetic model, Eq. (1). Fitting Eq. (3) to Al-19 and AZ-102 data required two terms, one corresponding to the initial reaction-controlled phase ending at approximately 700 °C (see Fig. 5) and the other to the final diffusion-controlled phase (see Section 3). Eq. (3) fitted NG-Fe2 and AN-105 with just a single term, reflecting a negligeable difference between the kinetics of the initial and final stages of silica dissolution. Fitted parameters of the empirical function, Eq. (3), and kinetic models, Eq. (6), are listed in Tables 1 and 2, respectively. Fig. 7 displays the fraction of dissolved silica as a function of temperature and heating rate together with fitted lines of the kinetic model.

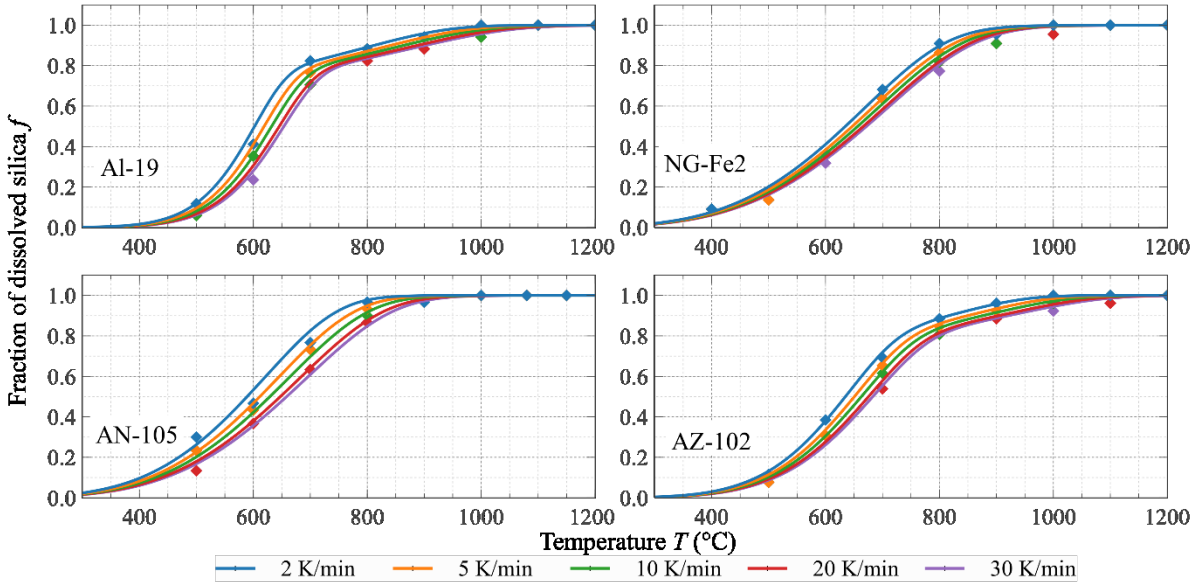

Figure 7. Fraction of dissolved silica. Points show experimental data. Lines represent the kinetic model.

Table 1. Fitted parameters of Eq. (3) and the coefficient of determination, R^2.

	Al-19	NG-Fe2	AN-105	AZ-102
	0.727	1	1	0.790
(K)	891.1	968.2	923.3	929.4
	14.29	6.81	7.16	9.94
(K s^{-1})	12.24	48.62	23.40	14.18
(K)	1089.1	-	-	1123.6
	7.77	-	-	9.55
(K s^{-1})	4.47	-	-	3.58
	0.997	0.994	0.995	0.996

Table 2. Fitted parameters of the kinetic models and the coefficient of determination, R^2.

	Al-19	NG-Fe2	AN-105	AZ-102
(s^{-1})	9.51×10^{16}	3.67×10^{22}	1.02×10^{10}	1.38×10^{19}
(J mol^{-1})	3.44×10^{6}	5.05×10^{6}	2.46×10^{6}	4.06×10^{6}

	−2.75	−10.9	−4.66	−5.41
	1.58	2.79	1.69	2.07
(s^{-1})	1.88×10^{10}	-	-	1.18×10^{8}
(J mol^{-1})	3.00×10^{6}	-	-	2.55×10^{6}
	−4.35	-	-	−2.44
	1.68	-	-	1.39
	0.995	0.994	0.994	0.997

The shift of silica fraction to higher values with increasing heating rate, seen in Fig. 7, is considerably smaller in the LAW and HLW feeds than in a soda-lime batch studied by Ueda et al. [33]. The smaller effect of heating rate can be attributed to faster reaction (and dissolution) rates of smaller feed particles, especially silica, that are not affected by the thermal history as much as larger particles typically present in commercial batches.

4.6 Cold Cap Bottom Temperature

As stated in the introduction, the cold cap bottom temperature, T_B, affects the heat flux to the cold cap, which controls the rate of melting (see Section 5). In previous studies [23,34–36,43,51,52], T_B was determined for moderately foaming feeds as $T_B = T_{FM}$ and for extensively foaming feeds as the temperature when the secondary gases start to evolve. These estimates simultaneously provide probable bounds for T_B, as the primary foam inside the cold cap starts to collapse at T_{FM} but has likely collapsed before the onset of redox reactions, which produce secondary gases. The true value of T_B should lie somewhere on the collapsing segment of the FET curve. Also, the rule of placing T_B at the onset of secondary gas evolution is not completely satisfying, because its connection to the collapse of the primary foam is not fully understood; it fits many LAW feeds [36].

The silica dissolution is intricately linked to primary foam collapse through its effect on viscosity and foam stability. And since a kinetic model of silica dissolution can be easily constructed (Section 4.5), the goal of finding T_B can be equivalently restated as a goal of finding the fraction of dissolved silica at the cold cap bottom, f_B. When we further postulate that f_B is a constant regardless of heating rate, it allows us to evaluate T_B for any temperature history.

We used three methods to estimate the T_B: (A) using only FET and EGA data—defining it by the secondary peak for HLW feeds, and by the start of SO_2 evolution for LAW feeds (Fig. 8), (B) using only XRD data—defining it by the same constant fraction of dissolved silica for all feeds, and (C) using a combination of XRD, FET, and EGA data—defining it by the constant fraction of dissolved silica, , which was determined separately for each feed as the average of dissolved silica fractions at each tested temperature using the FET and EGA data in point (A). We will further denote these temperatures as $T_{B,A}$, $T_{B,B}$, and $T_{B,C}$.

The gray strip in Fig. 8 shows the extent of the foam layer, Fig. 1, as the temperature interval between and . Pink dashed lines indicate $T_{B,B}$, yellow dashed lines $T_{B,C}$. In the case of Al-19, $T_{B,B}$ and $T_{B,C}$ values lie between primary and secondary maxima on the FET curve (V/V_g). In the case of NG-Fe2, all three definitions of T_B are close to each other. In the case of AN-105, $T_{B,A}$ values are close to $T_{B,C}$ values ($T_{B,B}$ is irrelevant; see below). Finally, in the case of AZ-102, the values of $T_{B,B}$ and $T_{B,C}$ are close to each other.

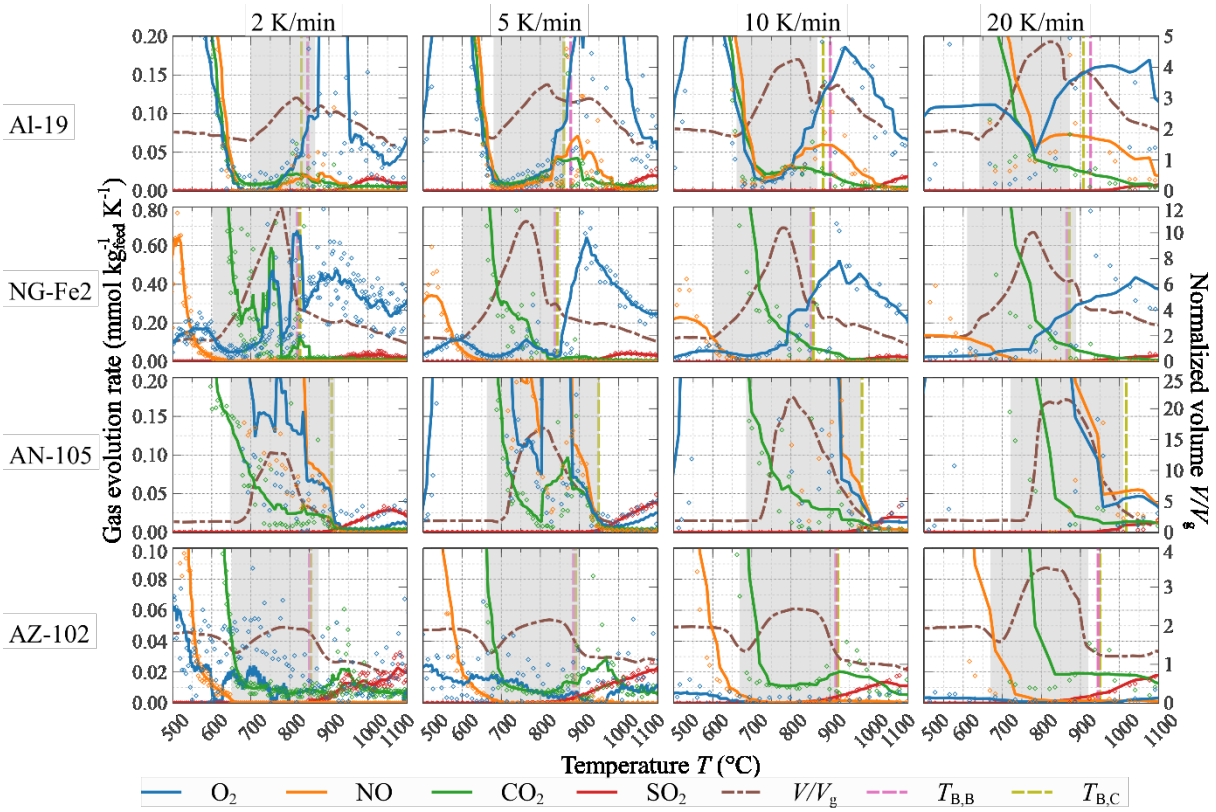

Figure 8. Gas evolution rate and normalized volume during primary foaming. Rows from top to bottom show Al-19, NG-Fe2, AN-105, and AZ-102. Columns from left to right show heating rates 2, 5, 10, and 20 K min^{-1}. The gray area highlights the temperature range .

Whereas the temperatures $T_{B,A}$ are different at each tested heating rate, the XRD data show that the fraction of dissolved silica at $T_{B,A}$ is almost constant (within a few percent). A similar result was obtained in a previous work focusing on container glass batches [33]. As shown in Fig. 9a, three out of the four feeds have dissolved silica fraction at $T_{B,A}$ close to (see the gray strip in Fig. 9a). This constant fraction is used to define temperature $T_{B,B}$. The dashed lines in Fig. 9a display the values of , the average fraction of dissolved silica at $T_{B,A}$. The average values of are also listed in Table 3 and used to define $T_{B,C}$. Fig. 9b shows $T_{B,A}$, $T_{B,B}$, and $T_{B,C}$ as a function of heating rate. The values of $T_{B,B}$ and $T_{B,C}$ are close to each other for Al-19, NG-Fe2, and AZ-102 feeds, as their values are close to 0.925 (see Table 3). The scatter of data points around the averages (dashed lines) in Fig. 9a can be attributed to uncertainties associated with the FET and EGA methods.

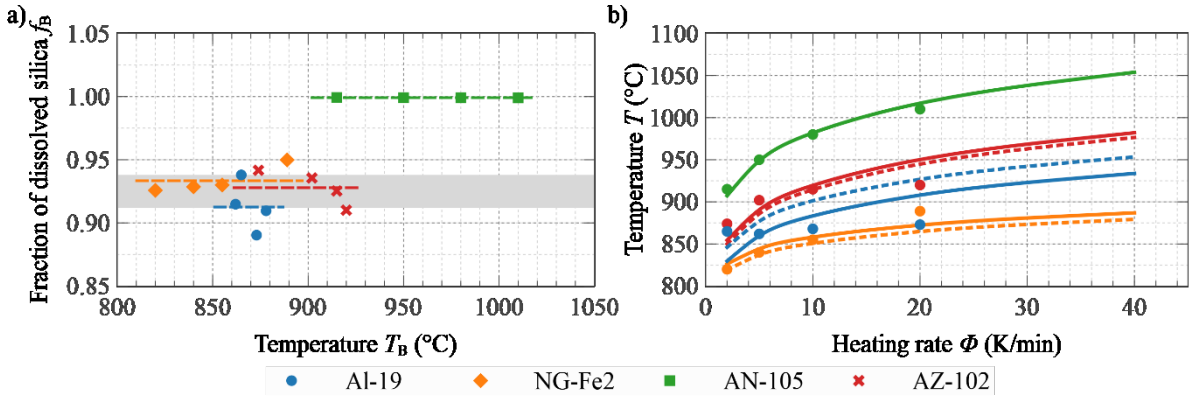

Figure 9. (a) Fraction of dissolved silica (f_B) at temperature for heating rates 2, 5, 10, and 20 K min^{-1}. Dashed lines represent average values for each feed. (b) $T_{B,A}$ (points), $T_{B,B}$ (dotted lines), and $T_{B,C}$ (solid lines) versus heating rate.

Table 3. Estimated values of fraction of dissolved silica at the cold cap bottom, .

	Al-19	NG-Fe2	AN-105	AZ-102
	0.913	0.934	0.996	0.928

4.7 Melt Viscosity

The interface between the cold cap and the melt is located where the primary foam collapses and where the predominantly vertical motion of the material within the cold cap turns to predominantly horizontal motion of the circulating melt below. This transition is likely controlled by the viscosity of the glass-forming phase, its homogeneity, and the presence of solid particles and gas bubbles.

The viscosity of the glass-forming melt affects the foam onset temperature, maximum foam height, and foam stability. For the viscosity at temperatures where Pa s, the viscosity of the amorphous phase is given by the Arrhenius equation [62]:

(8)

where is a constant coefficient and is the composition-dependent activation energy. We also use Eq. (8) for Pa s, even though the Arrhenius equation underestimates the viscosity value.

The temperature-dependent composition of the amorphous phase was obtained using the component mass balance in the form [23]

(9)

where is the *i*th component mass fraction in the amorphous phase, is the *i*th component mass fraction in the final glass, is the number of crystalline phases detected by the XRD, is the mass fraction of the *j*th crystalline phase as detected by XRD, and is the *i*th component mass fraction in the *j*th crystalline phase.

We estimated the viscosity of the amorphous phase using the Arrhenius equation. Models for glass melt viscosity are available for both for HLW [63] and LAW [64] glasses. Fig. 10 shows the amorphous phase viscosity by the HLW Model B and the LAW Model A, and the amorphous phase fraction by XRD as functions of temperature. At any temperature, the viscosity is lower for the two HLW feeds (Al-19, NG-Fe2) than for the two LAW feeds (AN-105, AZ-102). This could be attributed to the smaller fraction of silica in the HLW feeds. The largest difference in the total amorphous

fraction between HLW and LAW feeds was observed at 600 °C, where LAW feeds contained a higher fraction of solid phase consisting of silica, crystalline aluminosilicates, and zirconium oxide.

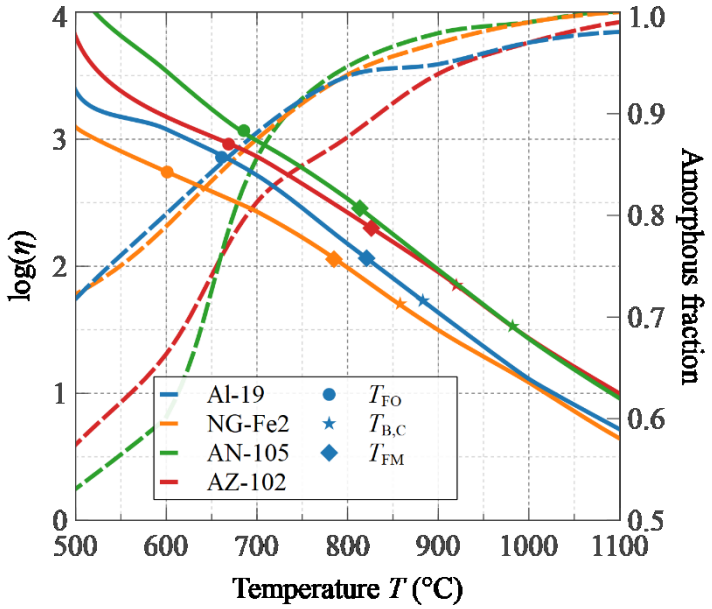

Figure 10. Estimated decadic logarithm of viscosity of amorphous phase (in Pa s), amorphous fraction, and characteristic temperatures, , , and, corresponding to 10 K min^{-1} heating rate.

Accordingly, because generally occurs at lower temperatures for feeds with a lower viscosity and a higher amorphous phase fraction, LAW feeds started foaming at higher temperatures than HLW feeds. In agreement with a recent study [23], the viscosity at was similar for the two investigated HLW feeds. However, it was smaller than the viscosity of the two LAW feeds, which suggests that other aspects, like the amount of released gas, play significant roles. Moreover, it was recently reported that the change in granulometry or source materials (while keeping the composition of the final glass unchanged) can change the of the feed by as much as 100 °C [48,53,55].

The values of the estimated amorphous phase viscosity at lie in a narrow range of 54 to 71 Pa s for the moderately foaming feeds. For the vigorously foaming feed, AN-105, the amorphous phase viscosity at was somewhat lower, 34 Pa s, likely because of the ongoing gas evolution that counteracted the gas release at higher viscosities (lower temperatures). The conditions at require further investigation into the role of foam rheology, as that may better define the interface between the cold cap and the free-flowing melt.

5. Discussion

The cold cap bottom temperature, T_B, affects the glass production rate, (the rate of melting). The semiempirical melting rate correlation expresses the relationship between and T_B as follows [35]:

(10)

where is the melt pool depth, is the bubbling rate (volumetric gas flow rate per melt area), is the melt density, is the melt viscosity, is the melter operating temperature, is the conversion enthalpy, and and are fitting coefficients. With all other parameters constant, the glass production rate increases as

the cold cap bottom temperature decreases.

However, the relationship between and T_B is more subtle. Changes in j produced by changes of other variables, such as , , or , affect the value of T_B. As j increases, the feed experiences faster heating, typically leading to an increase in T_B. Through this feedback, the conversion kinetics tends to counteract the intended increase in the melting rate [32]. This tendency is reminiscent of Le Chatelier's principle, according to which a change in physical and chemical conditions counteracts the resulting change in chemical equilibrium. But this principle is not necessarily applicable to a steady state [43].

The effect of T_B on j and the countereffect of j on T_B are important for melter modeling because T_B is the temperature at which the CFD model and the cold cap model interface. This poses two problems. One is the interface position and the other is the T_B value.

Although the boundary between the cold cap and the melt (the cold cap bottom) is approximated as a sharp interface, the real cold cap bottom is rather dynamic, as it is located at the edge of the collapsing primary foam where the gas phase and the liquid phase separate and the gas is carried away with the circulating flow of molten glass as shown in Fig. 1. The interface can be defined hydrodynamically as the point of change in the direction of motion from vertical to horizontal. This is a major change, considering that with the melting rate of 2500 kg m^{-2} d^{-1} the vertical melt velocity at the cold cap bottom is of the order 10^{-5} m s^{-1} while the circulation flow velocity is of the order of 10^{-1} m s^{-1} [65]. This change coexists with the change from the low density of primary foam to a higher density of bubbly melt below and is associated with critical rheological properties, including the glass-forming melt viscosity.

Since the melter feed during its conversion to molten glass is a complex, chemically reacting mixture, the cold cap bottom is located where the conversion degree reaches a high, well-defined value. Hence, chemical thermodynamics and the reaction kinetics place the interface at the kinetically determined .

Although these definitions, whether based on hydrodynamics, material properties, rheology, or chemical thermodynamics, are basically equivalent, so far only fitting Eq. (10) to reported averaged melting rates [35,36] has provided a rough validation for estimates. Regardless of how the cold cap bottom is determined, checking its position through direct measurements of temperature, velocity, or density fields in the cold cap bottom region remains impracticable. To assess , we must rely on laboratory tests with feed samples. Such tests do not measure directly; instead, they measure various feed properties, such as normalized volume, gas evolution, silica dissolution, or viscosity, as they respond to increasing temperature. Even though the cold cap bottom temperature is then estimated based on plausible criteria, its value is subject to considerable uncertainties.

The prime example is the FET, as it ties directly to the primary foam collapse. The condition proved valuable for moderately foaming HLW feeds but failed for vigorously foaming LAW feeds, for which . Its accuracy is being questioned because of the differences in the modes of foam collapse between the laboratory sample and the cold cap. Whereas foam collapses to the atmosphere in the feed samples, it occurs within the melt under the cold cap. Also, it is unfeasible to reproduce in the laboratory the temperature history the feed experiences in the cold cap. Since constant heating rates are used, the kinetic analysis is performed to determine the effects of nonlinear thermal histories (see Section 3).

Evolved gas analysis provides promising results for vigorously foaming LAW feeds but the connection between the onset of secondary gas-evolving reactions and the cold cap bottom is still unclear; that point was chosen mainly because it produced acceptable correlation with experimentally

measured melting rates using Eq. (10). Evolution of the secondary gases depends on the feed redox. Secondary gases would not appear in melts from heavily oxidized feeds, which is the case when nitrates are present. They can appear after NO_x gases escape. However, CO_2 can still be produced as a primary foaming gas. On the other hand, secondary O_2 would not evolve from a reduced melt; in this case, SO_2 may be generated, but its onset may be delayed and not mark the end of primary foaming.

The dissolved silica fraction measured using XRD was adopted as the conversion degree in this study. The temperature at which the silica fraction decreased to a small, fixed fraction was postulated equal to T_B. This constant fraction of dissolved silica, though independent of the temperature history, does not take on a universal value but must be determined on a per-feed basis with the help of FET and EGA data. Thus, uncertainties associated with the silica criterion persist and require further verification.

Finally, although the results with amorphous phase viscosity are encouraging, they must be tested with more feeds. The effects of foam rheology and foam stability merit further investigation.

All the above methods have limitations. Their success will be checked by the completion of the CFD melter model coupled with a kinetic submodel of the cold cap that is currently being developed. The preliminary results will be presented in a separate communication.

6. Conclusions

Several interdependent processes involved in the batch-to-glass conversion, including gas evolution, dissolution of solid particles, and foam kinetics, were studied using TGA, FET, EGA, and XRD for two HLW and two LAW simulated feeds. The strong dependence of the conversion processes on the heating rate suggested that the feed thermal history plays an important role during melting. Measured data were used to evaluate parameters of the kinetic model for the silica dissolution based on the Šesták-Berggren equation. Such a model can be used to track the conversion degree inside the cold cap and to determine the cold cap bottom temperature, , if the fraction of the dissolved silica at cold cap bottom, , is known. We recommend using a feed-specific for cold cap modeling purposes.

Acknowledgments

This work was supported by the U.S. Department of Energy's Waste Treatment & Immobilization Plant Project of the Office of River Protection. Richard Pokorný, Jaroslav Kloužek, and Miroslava Vernerová acknowledge financial support from the Czech Science Foundation (project No. 19-14179S). We are grateful to Jaehun Chun for expertly reviewing and Maura Zimmerschied for meticulously editing the manuscript.

References

[1] Choudhary MK, Venuturumilli R, Hyre MR. Mathematical Modeling of Flow and Heat Transfer Phenomena in Glass Melting, Delivery, and Forming Processes. Int J Appl Glas Sci [Internet]. 2010;1:188–214. Available from: http://doi.wiley.com/10.1111/j.2041-1294.2010.00018.x.

[2] Jebava M, Němec L. Role of Glass Melt Flow in Container Furnace Examined by Mathematical Modelling. Ceram - Silikaty [Internet]. 2018;62:86–96. Available from: http://www.ceramics-silikaty.cz/index.php?page=cs_detail_doi&id=1123.

[3] Li H, Xing Z, Xu S, et al. 3D Simulation of Borosilicate Glass All-Electric Melting Furnaces. Mauro J, editor. J Am Ceram Soc [Internet]. 2014;97:141–149. Available from:

http://doi.wiley.com/10.1111/jace.12597.
[4] Zhou J, Takahashi H, Tsuzuki N, et al. Investigation of Flow Behavior of Joule-Heating Flow in a 2-D Model of a Reprocessing Glass Melter Cavity. J Flow Control Meas Vis [Internet]. 2018;06:199–216. Available from: http://www.scirp.org/journal/doi.aspx?DOI=10.4236/jfcmv.2018.64016.
[5] Li L, Han J, Lin H, et al. Simulation of glass furnace with increased production by increasing fuel supply and introducing electric boosting. Int J Appl Glas Sci [Internet]. 2020;11:170–184. Available from: https://onlinelibrary.wiley.com/doi/abs/10.1111/ijag.13907.
[6] Suneel G, Kaushik CP, Satya Sai PM, et al. Enhancement of Glass Production Rate in Joule Heated Ceramic Melter. Chem Prod Process Model [Internet]. 2019; Available from: http://www.degruyter.com/view/j/cppm.ahead-of-print/cppm-2019-0068/cppm-2019-0068.xml.
[7] Suneel G, Satya Sai PM, Kaushik CP, et al. Experimental Investigation and Numerical Modeling of a Joule-Heated Ceramic Melter for Vitrification of Radioactive Waste. J Hazardous, Toxic, Radioact Waste [Internet]. 2019;23:04018035. Available from: http://ascelibrary.org/doi/10.1061/%28ASCE%29HZ.2153-5515.0000429.
[8] Schill P, Chmelar J. Use of computer flow dynamics in glass technology. J Non Cryst Solids [Internet]. 2004;345–346:771–776. Available from: https://linkinghub.elsevier.com/retrieve/pii/S0022309304008099.
[9] Mase H, Oda K. Mathematical model of glass tank furnace with batch melting process. J Non Cryst Solids [Internet]. 1980;38–39:807–812. Available from: https://linkinghub.elsevier.com/retrieve/pii/0022309380905360.
[10] Pokorný R, Hrma P, Lee S, et al. Modeling batch melting: Roles of heat transfer and reaction kinetics. J Am Ceram Soc [Internet]. 2020;103:701–718. Available from: https://onlinelibrary.wiley.com/doi/abs/10.1111/jace.16898.
[11] Dixon DR, Schweiger MJ, Riley BJ, et al. Temperature Distribution within a Cold Cap during Nuclear Waste Vitrification. Environ Sci Technol [Internet]. 2015;49:8856–8863. Available from: http://pubs.acs.org/doi/10.1021/acs.est.5b00931.
[12] Hujová M, Klouzek J, Cutforth DA, et al. Cold-cap formation from a slurry feed during nuclear waste vitrification. Ceram Int [Internet]. 2019;45:6405–6412. Available from: https://linkinghub.elsevier.com/retrieve/pii/S0272884218335089.
[13] Luksic SA, Pokorny R, George J, et al. In situ characterization of foam morphology during melting of simulated waste glass using x-ray computed tomography. Ceram Int [Internet]. 2020;46:17176–17185. Available from: https://linkinghub.elsevier.com/retrieve/pii/S0272884220305411.
[14] Guillen DP, Abboud AW, Eaton WC, et al. Melter Modeling over a Range of Scales to Support Vitrification at the WTP. Waste Manag Symp [Internet]. 2019. p. 13. Available from: https://www.osti.gov/biblio/1495093-melter-modeling-over-range-scales-support-vitrification-wtp.
[15] Guillen DP, Abboud AW, Pokorny R, et al. Development of a Validation Approach for an Integrated Waste Glass Melter Model. Nucl Technol [Internet]. 2018;203:244–260. Available from: https://www.tandfonline.com/doi/full/10.1080/00295450.2018.1458559.
[16] Abboud A, Guillen DP, Pokorny R. Heat Transfer Model of a Small-Scale Waste Glass Melter with Cold Cap Layer. 11th Int Top Meet Nucl Therm Hydraul [Internet]. 2016. p. 15. Available from: https://www.osti.gov/biblio/1367686-heat-transfer-model-small-scale-waste-glass-melter-cold-cap-layer.
[17] Abboud AW, Guillen DP. A methodology to reduce the computational cost of transient multiphysics simulations for waste vitrification. Comput Chem Eng [Internet]. 2018;115:64–80. Available from: https://linkinghub.elsevier.com/retrieve/pii/S0098135418302357.
[18] Abboud AW, Guillen DP, Pokorny R. Effect of Glass Viscosity on Foaming Behavior and Heat Transfer in a Laboratory Scale Waste Glass Melter. Int Top Meet Adv Therm Hydraul [Internet]. 2018. p. 15. Available from: https://www.ans.org/pubs/proceedings/article-45019/.
[19] Abboud AW, Guillen DP, Pokorny R. Effect of cold cap coverage and emissivity

on the plenum temperature in a pilot-scale waste vitrification melter. Int J Appl Glas Sci [Internet]. 2020;11:357–368. Available from: https://onlinelibrary.wiley.com/doi/abs/10.1111/ijag.15031.
[20] McCarthy BP, George JL, Dixon DR, et al. Rheology of simulated radioactive waste slurry and cold cap during vitrification. J Am Ceram Soc [Internet]. 2018;101:5020–5029. Available from: https://onlinelibrary.wiley.com/doi/abs/10.1111/jace.15755.
[21] Marcial J, Pokorný R, Kloužek J, et al. Effect of water vapor and thermal history on nuclear waste feed conversion to glass. Int J Appl Glas Sci [Internet]. 2021;12:145–157. Available from: https://onlinelibrary.wiley.com/doi/10.1111/ijag.15803.
[22] Hrma P, Goles CE, Yasuda DD. Drainage of Primary Melt in a Glass Batch. Ceram Trans. 1991;23:361–367.
[23] Lee SM, McCarthy BP, Hrma P, et al. Viscosity of glass-forming melt at the bottom of high-level waste melter-feed cold caps: Effects of temperature and incorporation of solid components. J Am Ceram Soc [Internet]. 2020;103:1615–1630. Available from: https://onlinelibrary.wiley.com/doi/abs/10.1111/jace.16876.
[24] Xu K, Hrma P, Rice JA, et al. Conversion of Nuclear Waste to Molten Glass: Cold-Cap Reactions in Crucible Tests. Vance E, editor. J Am Ceram Soc [Internet]. 2016;99:2964–2970. Available from: http://doi.wiley.com/10.1111/jace.14310.
[25] Pokorný R, Pierce DA, Hrma P. Melting of glass batch: Model for multiple overlapping gas-evolving reactions. Thermochim Acta [Internet]. 2012;541:8–14. Available from: https://linkinghub.elsevier.com/retrieve/pii/S0040603112001943.
[26] Suneel G, Rajasekaran S, Selvakumar J, et al. Determination of reaction kinetics during vitrification of radioactive liquid waste for different types of base glass. Nucl Eng Technol [Internet]. 2019;51:746–754. Available from: https://linkinghub.elsevier.com/retrieve/pii/S1738573318305485.
[27] Bodalbhai L, Hrma P. The dissolution of silica grains in isothermally heated batches of sodium carbonate and silica sand. Glas Technol. 1986;27:72–78.
[28] Pokorny R, Rice JA, Crum J V., et al. Kinetic model for quartz and spinel dissolution during melting of high-level-waste glass batch. J Nucl Mater [Internet]. 2013;443:230–235. Available from: https://linkinghub.elsevier.com/retrieve/pii/S0022311513009276.
[29] Narsimhan G, Ruckenstein E. Effect of bubble size distribution on the enrichment and collapse in foams. Langmuir [Internet]. 1986;2:494–508. Available from: https://pubs.acs.org/doi/abs/10.1021/la00070a020.
[30] Kim D-S, Hrma P. Foaming in Glass Melts Produced by Sodium Sulfate Decomposition under Ramp Heating Conditions. J Am Ceram Soc [Internet]. 1992;75:2959–2963. Available from: https://onlinelibrary.wiley.com/doi/10.1111/j.1151-2916.1992.tb04371.x.
[31] Kim D-S, Dutton BC, Hrma PR, et al. Effect of furnace atmosphere on E-glass foaming. J Non Cryst Solids [Internet]. 2006;352:5287–5295. Available from: https://linkinghub.elsevier.com/retrieve/pii/S0022309306011306.
[32] Ferkl P, Hrma P, Kloužek J, et al. Model for batch-to-glass conversion: coupling the heat transfer with conversion kinetics. J Asian Ceram Soc [Internet]. 2021;9:652–664. Available from: https://www.tandfonline.com/doi/full/10.1080/21870764.2021.1907914.
[33] Ueda N, Vernerová M, Kloužek J, et al. Conversion kinetics of container glass batch melting. J Am Ceram Soc [Internet]. 2021;104:34–44. Available from: https://onlinelibrary.wiley.com/doi/abs/10.1111/jace.17406.
[34] Hrma P, Pokorny R, Lee S, et al. Heat transfer from glass melt to cold cap: Melting rate correlation equation. Int J Appl Glas Sci [Internet]. 2019;10:143–150. Available from: http://doi.wiley.com/10.1111/ijag.12666.
[35] Lee S, Ferkl P, Pokorny R, et al. Simplified melting rate correlation for radioactive waste vitrification in electric furnaces. J Am Ceram Soc [Internet]. 2020;103:5573–5578. Available from: https://onlinelibrary.wiley.com/doi/abs/10.1111/jace.17281.
[36] Lee S, Cutforth DA, Mar D, et al. Melting rate correlation with batch properties and melter operating conditions during conversion of nuclear waste melter feeds to

glasses. Int J Appl Glas Sci [Internet]. 2021;12:398–414. Available from: https://onlinelibrary.wiley.com/doi/10.1111/ijag.15911.
[37] Kruger AA, Pegg IL, Chaudhuri M, et al. Melt Rate Enhancement for High Aluminum HLW Glass Formulation, VSL-08R1360-1, Rev. 0 [Internet]. Richland, WA (United States); 2013. Available from: http://www.osti.gov/servlets/purl/1105973/.
[38] Kruger AA, Gan H, Joseph I, et al. Melter Throughput Enhancements for High-Iron HLW, VSL-12R2490-1 [Internet]. Richland, WA (United States); 2012. Available from: http://www.osti.gov/servlets/purl/1059419/.
[39] Kruger AA, Muller IS, Gong W, et al. DuraMelter 100 Tests to Support LAW Glass Formulation Correlation Development, VSL-06R6480-1, Rev. 0 [Internet]. Richland, WA (United States); 2013. Available from: http://www.osti.gov/servlets/purl/1109494/.
[40] Muller IS, Pegg IL, McKeown DA, et al. LAW Glass Formulation to Support AZ-102 Actual Waste Testing, VSL-03R3470-1, Rev. 0. Washington, DC; 2003.
[41] Hujova M, Pokorny R, Klouzek J, et al. Foaming during nuclear waste melter feeds conversion to glass: Application of evolved gas analysis. Int J Appl Glas Sci [Internet]. 2018;9:487–498. Available from: http://doi.wiley.com/10.1111/ijag.12353.
[42] Hilliard Z, Hrma P. A Method for Determining Bulk Density, Material Density, and Porosity of Melter Feed During Nuclear Waste Vitrification. Vance E, editor. J Am Ceram Soc [Internet]. 2016;99:98–105. Available from: https://onlinelibrary.wiley.com/doi/abs/10.1111/jace.13919.
[43] Lee SM, Hrma P, Pokorny R, et al. Heat transfer from glass melt to cold cap: Effect of heating rate. Int J Appl Glas Sci [Internet]. 2019;10:401–413. Available from: https://onlinelibrary.wiley.com/doi/abs/10.1111/ijag.13104.
[44] Šesták J, Berggren G. Study of the kinetics of the mechanism of solid-state reactions at increasing temperatures. Thermochim Acta [Internet]. 1971;3:1–12. Available from: https://linkinghub.elsevier.com/retrieve/pii/0040603171850517.
[45] Šesták J. Šesták–Berggren equation: now questioned but formerly celebrated—what is right. J Therm Anal Calorim [Internet]. 2017;127:1117–1123. Available from: http://link.springer.com/10.1007/s10973-015-4998-x.
[46] Marcial J, Chun J, Hrma P, et al. Effect of Bubbles and Silica Dissolution on Melter Feed Rheology during Conversion to Glass. Environ Sci Technol [Internet]. 2014;48:12173–12180. Available from: https://pubs.acs.org/doi/10.1021/es5018625.
[47] Chun J, Pierce DA, Pokorný R, et al. Cold-cap reactions in vitrification of nuclear waste glass: Experiments and modeling. Thermochim Acta [Internet]. 2013;559:32–39. Available from: https://linkinghub.elsevier.com/retrieve/pii/S0040603113000932.
[48] Marcial J, Kloužek J, Vernerová M, et al. Effect of Al and Fe sources on conversion of high-level nuclear waste feed to glass. J Nucl Mater [Internet]. 2021;153423. Available from: https://linkinghub.elsevier.com/retrieve/pii/S0022311521006437.
[49] Cable M. Possibilities of progress in glass melting. J Non Cryst Solids [Internet]. 1985;73:451–461. Available from: https://linkinghub.elsevier.com/retrieve/pii/0022309385903680.
[50] Tooley F. Raw materials. Handb Glas Manuf. 2nd ed. New York, NY: Books for Industry; 1974. p. 19–54.
[51] Lee S, Hrma P, Pokorny R, et al. Glass production rate in electric furnaces for radioactive waste vitrification. J Am Ceram Soc [Internet]. 2019;102:5828–5842. Available from: https://onlinelibrary.wiley.com/doi/abs/10.1111/jace.16463.
[52] Hrma P, Klouzek J, Pokorny R, et al. Heat transfer from glass melt to cold cap: Gas evolution and foaming. J Am Ceram Soc [Internet]. 2019;102:5853–5865. Available from: https://onlinelibrary.wiley.com/doi/abs/10.1111/jace.16484.
[53] Lee S, Hrma P, Pokorny R, et al. Effects of alumina sources (gibbsite, boehmite, and corundum) on melting behavior of high-level radioactive waste melter feed. MRS Adv [Internet]. 2017;2:603–608. Available from: https://www.cambridge.org/core/product/identifier/S2059852116006447/type/journal_article.
[54] Lee S, Hrma P, Pokorny R, et al. Effect of melter feed foaming on heat flux to the

cold cap. J Nucl Mater [Internet]. 2017;496:54–65. Available from: https://linkinghub.elsevier.com/retrieve/pii/S0022311517304208.
[55] Lee S, VanderVeer BJ, Hrma P, et al. Effects of heating rate, quartz particle size, viscosity, and form of glass additives on high-level waste melter feed volume expansion. J Am Ceram Soc [Internet]. 2017;100:583–591. Available from: https://onlinelibrary.wiley.com/doi/abs/10.1111/jace.14629.
[56] Xu K, Hrma P, Rice J, et al. Melter Feed Reactions at T ≤ 700°C for Nuclear Waste Vitrification. Vance E, editor. J Am Ceram Soc [Internet]. 2015;98:3105–3111. Available from: https://onlinelibrary.wiley.com/doi/abs/10.1111/jace.13766.
[57] Nienhuis E, Saleh M, McCloy J. Structural Characterization of Ternary Salt Melts for Low Activity Waste Applications. MRS Adv [Internet]. 2019;4:1045–1056. Available from: http://link.springer.com/10.1557/adv.2019.136.
[58] Pierce DA, Hrma P, Marcial J, et al. Effect of Alumina Source on the Rate of Melting Demonstrated with Nuclear Waste Glass Batch. Int J Appl Glas Sci [Internet]. 2012;3:59–68. Available from: https://onlinelibrary.wiley.com/doi/10.1111/j.2041-1294.2012.00079.x.
[59] Jin T, Chun J, Dixon DR, et al. Melter feed viscosity during conversion to glass: Comparison between low-activity waste and high-level waste feeds. J Am Ceram Soc [Internet]. 2018;101:1880–1891. Available from: https://onlinelibrary.wiley.com/doi/abs/10.1111/jace.15352.
[60] Jin T, Mar D, Kim D, et al. Reactions during conversion of simplified low-activity waste glass feeds. Thermochim Acta [Internet]. 2020;694:178783. Available from: https://linkinghub.elsevier.com/retrieve/pii/S0040603120306985.
[61] Hrma P. Crystallization during processing of nuclear waste glass. J Non Cryst Solids [Internet]. 2010;356:3019–3025. Available from: https://linkinghub.elsevier.com/retrieve/pii/S0022309310003753.
[62] Hrma P, Kruger AA. High-temperature viscosity of many-component glass melts. J Non Cryst Solids [Internet]. 2016;437:17–25. Available from: https://linkinghub.elsevier.com/retrieve/pii/S0022309316300102.
[63] Hrma P, Han S-S. Effect of glass composition on activation energy of viscosity in glass-melting-temperature range. J Non Cryst Solids [Internet]. 2012;358:1818–1829. Available from: https://linkinghub.elsevier.com/retrieve/pii/S0022309312002918.
[64] Ferkl P, Hrma P, Kruger A. Parsimonious viscosity-composition relationships for high-temperature multicomponent glass melts. J Asian Ceram Soc. 2021;Accepted.
[65] Abboud AW, Guillen DP, Hrma P, et al. Heat transfer from glass melt to cold cap: Computational fluid dynamics study of cavities beneath cold cap. Int J Appl Glas Sci [Internet]. 2021;12:233–244. Available from: https://onlinelibrary.wiley.com/doi/10.1111/ijag.15863.

Appendix

Table A1. Melter feed compositions in g to make 100 g of HLW glass or for 1 liter of LAW simulant with glass-forming and -modifying additives (GFMA).

Melter feed simulant	Al-19 Mass (g)	NG-Fe2 Mass (g)	AZ-102 Mass (g)	AN-105 Mass (g)
$Al(NO_3)_3$•9H2O			2.82	422.01
$Al(OH)_3$	36.90	8.61		35.22
H_3BO_3				0.45
$Na_2B_4O_7$•10H_2O		37.16		
Bi_2O_3	1.16			
CaO	1.10			
$CaCO_3$		0.94		

CeO_2		0.12		
Cr_2O_3•1.5H_2O	0.62	0.30		
Na2CrO_4•4H_2O			3.47	2.85
$Fe(OH)_3$	6.32	20.54		
$FePO_4$•2H_2O	2.79	1.71		
KNO_3	0.30			
KOH			10.13	8.25
$La(OH)_3$•3H_2O		0.11		
MgO	0.12			
$Mg(OH)_2$		0.24		
MnO_2		3.98		
NaOH	2.04	0.81	108.59	458.03
NiO			0.11	0.09
$Ni(OH)_2$	0.50	0.59		
PbO	0.41	0.63	0.11	0.09
SiO_2			0.37	0.34
$SrCO_3$		0.28		
NaCl			4.68	1.82
NaF	1.49		2.48	1.71
Na_3PO_4•12H_2O			9.39	7.68
Na_2SO_4			20.53	7.32
$NaNO_2$	0.35	0.01	35.70	128.79
$NaNO_3$	1.24	0.45	9.67	
Na_2CO_3			40.77	
$NaC_2H_3O_2$				5.24
$NaCHO_2$				3.26
$C_2H_4O_3$				2.73
$C_2H_2O_4$			3.21	
$H_2C_2O_4$•2H_2O	0.12	0.06		
GFMA	Mass (g)	Mass (g)	Mass (g)	Mass (g)
Al_2SiO_5			147.13	18.15
H_3BO_3	34.26	0.56	253.08	202.23
$CaSiO_3$	9.71		219.20	63.09
Fe_2O_3			71.22	60.14
Li_2CO_3	8.92	3.87	152.46	
Mg_2SiO_4			84.78	34.48
NaCl				
Na_2CO_3	10.66	4.04	34.18	
Na_2SiO_3		8.03		
Na_2SO_4	0.36	0.39		
SiO_2	22.11	37.33	465.92	446.62

TiO_2			21.08	16.92
ZnO	0.08	0.03	49.81	39.98
$ZrSiO_4$			64.55	51.69
$Zr(OH)_4 \bullet xH_2O$ (x = 0.654)	0.55	1.57		
$C_{12}H_{22}O_{11}$			12.26	78.50
Total	142.09	132.36	1827.70	2097.68

Table A2. Glass compositions in mass %.

Glass	Al-19	NG-Fe2	AZ-102	AN-105
Al_2O_3	23.97	5.58	6.07	5.97
B_2O_3	19.19	13.81	9.95	9.79
Bi_2O_3	1.14			
CaO	5.58	0.52	6.96	2.46
Ce_2O_3		0.11		
Cl			0.20	0.20
Cr_2O_3	0.52	0.26	0.08	0.08
F	0.67		0.08	0.08
Fe_2O_3	5.90	16.01	5.48	5.38
K_2O	0.14		0.54	0.54
La_2O_3		0.09		
Li_2O	3.57	1.55	4.26	
MgO	0.12	0.16	2.94	1.45
MnO		3.23		
Na_2O	9.58	14.17	5.72	21.27
NiO	0.40	0.47	0.01	0.01
P_2O_5	1.05	0.64	0.12	0.12
PbO	0.41	0.62	0.01	0.01
SO_3	0.20	0.22	0.80	0.41
SiO_2	27.00	41.05	48.92	44.50
SrO		0.19		
TiO_2			1.39	1.37
ZnO	0.08	0.03	3.48	3.43
ZrO_2	0.39	1.13	2.99	2.94
SUM	100	100	100	100